PCCP

Accepted Manuscript

ROYAL SOCIETY OF CHEMISTRY

www.rsc.org/pccp

The Transformation from Amorphous Iron Phosphate to Sodium Iron Phosphate in Sodium-ion Batteries

Yao Liu, [a] Yirong Zhou, [a] Junxi Zhang, [*a] Shiming Zhang, [ab] Shuojiong Xu.[a]

[a] *Shanghai Key Laboratory of Materials Protection and Advanced Materials in Electric Power, Shanghai University of Electric Power, Shanghai, 200090, People's Republic of China.*

[b] *State Key Laboratory of Silicon Materials, Key Laboratory of Advanced Materials and Applications for Batteries of Zhejiang Province &Department of Materials Science and Engineering, Zhejiang University, Hangzhou 310027, People's Republic of China.*

* Corresponding author. Tel. /Fax. : +86-21-35303677.

E-mail address: zhangjunxi@shiep.edu.cn.

Abstract: In this article, the structure and electrochemical performance of sodiated iron phosphate ($FePO_4$) synthesized by the micro-emulsion technique have been investigated by X-ray diffraction (XRD), high resolution transmission electron microscopy (HRTEM) and electrochemical measurement. The results reveal that amorphous $FePO_4$ could be transformed into crystallite sodium iron phosphate ($NaFePO_4$) during the electrochemical sodiation. Furthermore, the results of electrochemical testing show that the initial specific-discharge capacity of $FePO_4$ is 142mAh g^{-1} and it still delivers a reversible capacity of 130.8mAh g^{-1} after 120 cycles. The discharge capacities could attain values of 142mAh g^{-1}, 119.1mAh g^{-1}, 91.5mAh g^{-1} and 63.5mAh g^{-1} at 0.1C, 0.2C, 0.5C and 1C, respectively. These findings have indicated that $NaFePO_4$ has been formed during the electrochemical process and amorphous structure $FePO_4$ is one of the most promising "host" materials.

Keywords: Amorphous iron phosphate; Sodium iron phosphate; Sodium-ion batteries; X-ray diffraction; high resolution transmission electron microscopy.

Introduction

Sodium-ion batteries (SIBs) are considered a suitable alternative to current lithium-ion batteries (LIBs) on account of being potentially much cheaper and environmentally benign.[1-3] Sodium is located below lithium in the periodic table, and both of them show similar chemical properties in many respects. In theory, sodium-ions could shuttle between the positive and negative electrodes during charging and discharging in SIBs.[4-6] However, most of the "host" material of lithium-ion batteries may be not suitable for SIBs because the size of the sodium-ion radius is larger than that of the lithium ionic radius.[7] Hence, there is an important need to find a suitable electrode material for SIBs.

Since the reported by Padhi *et al.*[8] olivine $LiFePO_4$ has been attracting extensive attention as one of the most promising candidate of cathode material for lithium ion batteries.[9-13] Compared with olivine $LiFePO_4$, olivine $NaFePO_4$ is also feasible as the cathode material for SIBs.[14] However, $NaFePO_4$ has two main structures, namely maricite (Fig. 1a) and olivine (Fig. 1b), the olivine structure belongs to the orthorhombic frameworks (space group No. 62, Pnma). Orthorhombic frameworks are built from FeO_6 octahedral and PO_4 tetrahedral units with corner-sharing and edge-sharing arrangements.[15] In maricite, sodium-ions occupy the 4c Wyckoff sites and the ferrous-ion (Fe^{2+}) species are situated in 4a sites, which is the edge-sharing FeO_6 octahedra with no sodium-ion diffusion channels.[16] This structure of maricite $NaFePO_4$ has been shown electrochemically inactive.[7]

Up to date, using the synthetic method of olivine $LiFePO_4$ to synthesize $NaFePO_4$

mainly obtains $NaFePO_4$ with maricite structure .[17] The typical $NaFePO_4$ maricite phase seems to be the thermodynamically favorable phase because it is obtained at high temperature or in hydrothermal conditions. Therefore, it is inadvisable to synthesize olivine $NaFePO_4$ through the synthetic method of olivine $LiFePO_4$.[18] In previous reports, olivine $NaFePO_4$ was usually obtained by electrochemical Li-Na exchange of olivine $LiFePO_4$, but this method was very complex.[19]

The $LiFePO_4$ can deintercalate 1 molar lithium ion per formula unit during the charging process, corresponding to the phase transformation from $LiFePO_4$ phase to $FePO_4$ phase, which still maintains a similar structure.[20, 21] Therefore, it is possible to use $FePO_4$ as cathode material for rechargeable batteries with several advantages. Firstly, Fe^{3+} compounds are inexpensive and easily available raw materials. Moreover, the synthesis process of $FePO_4$ is simple, environmentally friendly and without protective atmosphere. Furthermore, $FePO_4$ as cathode material for rechargeable batteries has high theoretical capacity (178mAh g^{-1}).[8, 22-24]

In previous work, most researchers have focused on choosing the best synthetic method to get an excellent electrochemical performance for amorphous $FePO_4$ as cathode material. Fang *et al.*[25] reported that mesoporous amorphous $FePO_4$ nanospheres were synthesized as cathode material for SIBs with high performance through a chemically induced precipitation method. Xu *et al.*[26] used a micro-emulsion technique to fabricate maize-like amorphous FePO4/MCNT core-shell nanowire composites as the cathode material for SIBs. Liu *et al.*[27] reported that $FePO_4$ nanoparticles were grown on reduced oxide graphene to fabricate $FePO_4$/graphene

composite as cathode material for SIBs.

Recently, much attention has been focused on amorphous $FePO_4$, which is thought to be potential host material for SIBs.[28, 29] Most importantly, amorphous $FePO_4$ is different from other traditional cathode materials which are based on the mechanism of crystal structure and "guest ion" insertion/extraction during the charge/discharge process.[30, 31] Generally, these kinds of "host" material have limited ion channels for "guest ions". However, according to reports from some researchers, amorphous $FePO_4$ possesses unique benefits owing to its non-crystalline structure, such as short-range structural ordering, improved kinetics, a high surface area and free volume to accommodate lattice distortions without producing macroscopic phase transitions, which may ultimately improve the specific capacities and provide stable electrochemical cycling over a wide potential window.[32, 33] However, there has been rarely research about the mechanism and structure changes of amorphous $FePO_4$ during the electrochemical process.

In this article, the structural changes of amorphous $FePO_4$ during the sodium-ion insertion/de-insertion have been characterized by means of XRD and HRTEM. The results show that the sodium-ions are inserted into amorphous $FePO_4$ to fabricate crystallite $NaFePO_4$. This may be one of the most promising methods to synthesize the highly electrochemical activity of $NaFePO_4$ as cathode material for SIBs.

Experimental

Material preparation

The $FePO_4$ was synthesized by the micro-emulsion method. Two cyclohexane/Triton

X-100/n-butylalcohol micro-emulsion systems were prepared, labeled A and B, in a volume ratio of 5:3:1. 0.5mol/L $Fe(NO_3)_3 \cdot 9H_2O$ and $NH_4H_2PO_4$ were prepared, respectively. 100mL $Fe(NO_3)_3 \cdot 9H_2O$ and $NH_4H_2PO_4$ were added into micro-emulsion A and micro-emulsion B, and stirred magnetically for an hour. Then, both were transferred into a glass reaction kettle and ammonia was added dropwise to adjust the pH value to 2.6. The suspension continued to react at 45°C and pH 2.6 for 3h. After aging for 3 hours, the solution was centrifuged at 8000 r/min for 15 minutes, and washed three times with mixed alcohol and acetone (volume ratio of 1:1). Lastly, the resulting precipitates were dried at 100°C for 12 h, and then calcined in a tube furnace at 460°C for 3 h under an air atmosphere. In contrast, we obtained the crystal $FePO_4$ with same method, but the heat-treatment temperature is 650°C.

Characterization

Powder XRD patterns were measured using a Bruker D8 Advance X-ray diffractometer with Cu-Kα radiation, operating at 40kV and 40mA within the diffraction angle (2θ) from 20° to 90°, at a rate of 2°/min and step size of 0.02°. Thermogravimetry analysis and differential scanning calorimetry (TGA-DSC) were conducted using the STA 409 PC (Netzsch, Germany). The range of temperature increase was from room temperature to 800°C, at a rate of 10°C/min under air atmosphere. Scanning electron microscopy (SEM) images were obtained using the XL-30 FEG model (Philips, Holland). Transmission electron microscopy (TEM, JEM-2100; 200KeV) was used to study the micro-structure of the amorphous $FePO_4$.

Electrochemical measurement and characterization of structure change

The cathode electrode material was prepared by ball-milling with the ratio of active material, conductive material and PTFE (polytetra-fluoroethylene), at 62:30:8 in weight. The typical electrode mass was 15 mg. Electrochemical performance was evaluated with a CR-2016 type coin, consisting of the cathode material and a metallic-sodium anode, with 1 mol/L $NaClO_4$ in a mixture of ethylene carbonate/dimethyl carbonate (EC/DMC, 1:1 by volume), and with electrolyte and glass-fibre as separators. All coin batteries were assembled in an argon-filled glove box.

Galvanostatic cycling was tested in the voltage range of 1.5–4.2V, using a Land CT2001A battery test system (Wuhan Land, China). Cyclic voltammetry (CV) test was carried out on the electrochemical work station (Chenghua CHI660C, Shanghai, China) in the voltage window of 1.5–4.2V, at room temperature (25ºC). The CV scanning rate was 0.05 mV s^{-1}.

The XRD measurements of cathodic active materials were performed after electrochemical testing, when the negative electrodes were taken down from the test coin cells for XRD measurement. More specifically, the electrodes were taken down from decomposition of the coin cells, then rinsed with dimethyl carbonate/ethylene carbonate (DMC/EC, 1:1 by volume), to remove excess electrolyte. The electrode samples were dried at room temperature in a Mikrouna glove box filled with a highly purified argon atmosphere (moisture and oxygen contents lower than 1 ppm). The diffraction data obtained for diffraction angle (2θ) were from 3° to 90°, at a rate of 2°/min, with step size of 0.01°. HRTEM images with EDS and their corresponding

select area electron diffraction (SAED) images were obtained using the Tecnai G2 20 TWIN (FEI, America). The samples were ultrasonicated for an hour in ethanol to decrease agglomeration, then transferred to a porous carbon film-supported Cu mesh grid.

Result and discussion

Nano-particles of $FePO_4$ were synthesized by the micro-emulsion technique. This approach was quite different from the usual method, which is shown in Fig. 2. This unique system of water/oil could cause homogeneous nuclear growth of the $FePO_4$ nanoparticles in the micro-reactor.

Fig. 3 displays the TGA-DSC curves of the $FePO_4$ precursor. The weight loss took place below 250ºC and remained stable after 450ºC, which corresponded to the dehydration process of the precursor. The total weight loss was about 25.2% ($2.78H_2O$), which is close to the theoretical value for $FePO_4 \cdot 3H_2O$ (26.35%, 3.00 H_2O).[34] The DSC curve had two peaks located at about 120ºC and 560ºC, respectively, which corresponded to the endothermic peak of dehydration and exothermic peak of the crystal transfer process.[35]

The resulting precipitates were heat treated at 460°C, and then the nanospheres of amorphous $FePO_4$ were obtained. The XRD profile of as-prepared $FePO_4$ is shown in Fig. 4, which displays no signals of crystalline diffraction peaks. The results demonstrate an amorphous structure, which are consistent with previously reported.[36] The crystal structure $FePO_4$ was obtained through sintering at 650°C. The XRD pattern of $FePO_4$ at 650°C heat treatment is shown in Fig. 4. The peaks at 20.3°, 25.8°,

35.6°, 36.5°, 38°, 39.2°, 41.4°, 48.2°, 58.3°, 61.6°, 65.6° can be assigned to the (100), (102), (110), (104), (112), (200), (203), (106), (212), (116) and (206) facets of $FePO_4$ accordingly, which indicated the formation of hexagonal $FePO_4$ (JCPDS file No. 70-1793) [29].

The SEM images of as-prepared $FePO_4$ sintered at 460°C and 650°C are shown in Fig. 5a and Fig. 5b, respectively. The $FePO_4$ nanoparticles sintered at 460°C have a sphere-like morphology with a diameter of about 20nm. Compared with $FePO_4$ samples at 460°C, the size of the $FePO_4$ nanoparticles sintered at 650°C became much larger, which is attributed to more serious agglomeration and to crystal growth.The EDS analysis of $FePO_4$ is shown in Fig. 5c, proving that the ratio of Fe : P is near to 1 : 1 among the components of $FePO_4$.

The electrochemical performance of the amorphous $FePO_4$ as cathode material for SIBs is shown in Fig. 6. The result of the CV test is displayed in Fig. 6a. There is a pair of current peaks positioned at 2.53V and 2.09V, respectively, which could be corresponding to the redox of Fe^{2+}/Fe^{3+}.[27] The broad redox peaks indicate that the process of sodiation/desodiation is a continuous single-phase redox reaction, which is quite different from that of crystal electrode material. The discharge/charge curves of amorphous $FePO_4$ electrode are shown in Fig. 6b at various C-rates within the voltage window of 1.5-4.2V. The specific-discharge capacities attain values of 142mAh g^{-1}, 119.1mAh g^{-1}, 91.5mAh g^{-1} and 63.5mAh g^{-1} at 0.1C, 0.2C, 0.5C and 1C, respectively. The initial specific-discharge capacity of $FePO_4$ is 142mAh g^{-1} (Fig. 6c), up to 80% of the theoretical specific capacity (178 mAh g^{-1}). Furthermore, it still

maintains a reversible specific-discharge capacity of 130.8mAh g^{-1} after 120 cycles. The coulomb efficiency is near to 100% in all the cycles. The electrochemical performance of the hexagonal $FePO_4$ was shown in Fig. 6d. The discharge-specific capacity is 126.4 mAh g^{-1} and maintains at 86 mAh g^{-1} after the 30th cycle. The results indicated that amorphous $FePO_4$ showed outstanding electrochemical performance compared with hexagonal $FePO_4$.

The amorphous $FePO_4$ nanoparticles acted as cathode material for SIBs with excellent cycle performance and rate capability. However, the phenomenon of specific-discharge capacity fluctuation during the initial cycles (Fig. 6c, inset) may connect with the formation of $NaFePO_4$. For further research into the mechanism of amorphous $FePO_4$ as cathode material, XRD patterns of the $FePO_4$ cathode samples were taken from the separated sodium half cells until the half of discharge/charge and completed discharge/charge, as shown in Fig. 7. Compared with the XRD pattern of the amorphous $FePO_4$ as mentioned before, the XRD patterns of sodium-ions insertion show series of diffraction peaks (Fig. 7a). Except the diffraction peaks of graphite (26.8°) and steel (43.8°), the rest are corresponding to the diffraction peaks of the olivine structure $NaFePO_4$, which can indicate the formation of crystallite $NaFePO_4$. The phase composition of the samples and the lattice parameters of $NaFePO_4$ calculated by the Rietveld refinement method are listed in Table 1.[17] This observation indicates a transformation from amorphous to crystallitic during the sodium-ion insertion process. According to the diffuse-interface thermodynamic model,[37] the formation of crystallite $NaFePO_4$ describes the crystal growth from the

surface to the interior and is driven by the potential. The surficial crystallite films are formed at the initial stage and there is then gradual formation of crystallite $NaFePO_4$, which is also depended on the nucleation energy barriers. The XRD patterns of the $FePO_4$ cathode samples until the half of discharge/charge show the only peak at the scanning angle (2θ) of 20.21° which corresponds to the (101) diffraction plane of $NaFePO_4$. The (101) diffraction plane of $NaFePO_4$ is formed preferentially owing to the lowest nucleation energy barriers.[38] In contrast, we investgated the structure changes for hexagonal $FePO_4$ after process of sodiation. The XRD patterns hexagonal $FePO_4$ at the state of completed discharge are shown in Fig.8. The results suggested that the hexagonal $FePO_4$ displayed a diffraction peak of (101) plane of $NaFePO_4$ after the process of sodiation. Compared with the XRD pattern of sodiated $NaFePO_4$ from amorphous $FePO_4$, hexagonal $FePO_4$ did not appear the diffraction peak of (201) and (020) planes after sodiation. As we known, the sodium-ion diffusion takes place along the b-axis (010 direction) in the crystal structure of olivine $NaFePO_4$ (space group: *Pnma*) during the sodiation and desodiation process.[39] The results show that the amorphous $FePO_4$ could easier transform into high active $NaFePO_4$ compared with that of hexagonal $FePO_4$ in SIBs.

HRTEM images of sodiation/desodiation and EDS are shown in Fig. 9. The morphology of desodiation/sodiation exhibit in Fig. 9a and Fig. 9b, respectively. According to Fig. 9a and the SAED image (Fig. 9a, inset), there are no distinguishable lattice fringes or obvious diffraction rings, which indicates the amorphous structure of desodiation $FePO_4$. However, observation of the HRTEM image of sodiation $FePO_4$

(Fig. 9b, inset) shows obviously fringe widths with dimensions of 4.4Å corresponding to the (101) diffraction planes, which agrees well with XRD patterns of peaks at the diffraction angle of 20.21°, as mentioned before. The corresponding SAED pattern of sodiation of $FePO_4$ (Fig. 9b, inset) displays obvious diffraction rings. Therefore, the results support the existence of the amorphous-to-crystalline transition in nanoscale amorphous $FePO_4$ cathode material in SIBs during the electrochemical reaction. The EDS of the completed discharge amorphous $FePO_4$ is shown in Fig. 9c, which exhibits the stoichiometric composition of Na: Fe: P to be near 1:1:1. This result indicates that the component of the crystallite phase was $NaFePO_4$.

The XRD patterns of $FePO_4$ after many cycles of charging/discharging operation were shown in Fig.10, which displayed some diffraction peaks. According to the previous report[40, 41], the series of diffraction peaks were corresponding to the orthorhombic structure of $FePO_4$. The result indicated that amorphous $FePO_4$ had transformed into orthorhombic $FePO_4$ after many cycles of charging/discharging.

Fig. 11 schematically illustrates the amorphous to crystallite transition in amorphous $FePO_4$ as cathode material for SIBs during electrochemical sodium-ion insertion. The sodium-ions are inserted into the amorphous $FePO_4$ in the electrochemical process, and then crystallite $NaFePO_4$ is formed. The process of amorphous-to-crystalline transition during electrochemical cycling is decided by the changing potential.[42] According to the result of the electrochemical test, as mentioned before, the phenomenon of specific-discharge capacity fluctuation during the initial cycles corresponds to the process of the formation of crystallite $NaFePO_4$ and gradual

stability was resulted from the crystallite $NaFePO_4$ participating during the electrochemical reaction.

Conclusion

Amorphous $FePO_4$ was synthesized by the micro-emulsion technique, which could act as cathode material for SIBs with excellent cycle performance and rate capability. The structure transformation of $FePO_4$ nanoparticles during sodiation/desodiation has been investigated by XRD and HRTEM. The results show that the amorphous $FePO_4$ transforms into crystallite $NaFePO_4$ during the process of sodiation. These findings may offer a simple method to synthesize highly active $NaFePO_4$. Furthermore, the inexpensive and environmentally friendly amorphous $FePO_4$ nanoparticles cathode material may have considerable potential to be used as one of an insertion "host" material for a variety of ions with various atomic radii/charges, making it useful in energy-storage and electric vehicle applications.

Acknowledgements

This work was carried out with the financial support of the Shanghai Science & Technology Commission Project 13NM1401400, the Ability Development of Shanghai Science & Technology Commission Project 09230501400, and the Research Foundation of the Ministry of Education (No.20502). We thank Proof-Reading-Service.com (http://www.proof-reading-service.com/) for its linguistic assistance during the preparation of this manuscript.

References

1. V. Palomares, P. Serras, I. Villaluenga, K. B. Hueso, J. Carretero-Gonzalez and T. Rojo, *Energy & Environmental Science*, 2012, **5**, 5884-5901.
2. S.-W. Kim, D.-H. Seo, X. Ma, G. Ceder and K. Kang, *Advanced Energy Materials*, 2012, **2**, 710-721.
3. D. Larcher and J. M. Tarascon, *Nature Chemistry*, 2015, **7**, 19-29.
4. M. D. Slater, D. Kim, E. Lee and C. S. Johnson, *Advanced Functional Materials*, 2013, **23**, 947-958.
5. W. Song, X. Cao, Z. Wu, J. Chen, K. Huangfu, X. Wang, Y. Huang and X. Ji, *Physical Chemistry Chemical Physics*, 2014, **16**, 17681-17687.
6. D. H. Lee, J. Xu and Y. S. Meng, *Physical Chemistry Chemical Physics*, 2013, **15**, 3304-3312.
7. S. P. Ong, V. L. Chevrier, G. Hautier, A. Jain, C. Moore, S. Kim, X. Ma and G. Ceder, *Energy & Environmental Science*, 2011, **4**, 3680-3688.
8. A. K. Padhi, K. S. Nanjundaswamy and J. B. Goodenough, *Journal of The Electrochemical Society*, 1997, **144**, 1188-1194.
9. K. Saravanan, M. V. Reddy, P. Balaya, H. Gong, B. V. R. Chowdari and J. J. Vittal, *Journal of Materials Chemistry*, 2009, **19**, 605-610.
10. M. Park, X. Zhang, M. Chung, G. B. Less and A. M. Sastry, *Journal of Power Sources*, 2010, **195**, 7904-7929.
11. X. Zhu, J. Hu, W. Wu, W. Zeng, H. Dai, Y. Du, Z. Liu, L. Li, H. Ji and Y. Zhu, *Journal of Materials Chemistry A*, 2014, **2**, 7812-7818.
12. J. Song, L. Wang, G. Shao, M. Shi, Z. Ma, G. Wang, W. Song, S. Liu and C. Wang, *Physical Chemistry Chemical Physics*, 2014, **16**, 7728-7733.
13. Q. Huang, H. Li, M. Gratzel and Q. Wang, *Physical Chemistry Chemical Physics*, 2013, **15**, 1793-1797.
14. K. Zaghib, J. Trottier, P. Hovington, F. Brochu, A. Guerfi, A. Mauger and C. M. Julien, *Journal of Power Sources*, 2011, **196**, 9612-9617.
15. A. Whiteside, C. A. J. Fisher, S. C. Parker and M. Saiful Islam, *Physical Chemistry Chemical Physics*, 2014, **16**, 21788-21794.
16. C. M. Burba and R. Frech, *Spectrochimica Acta Part A: Molecular and Biomolecular Spectroscopy*, 2006, **65**, 44-50.
17. J. N. Bridson, S. E. Quinlan and P. R. Tremaine, *Chemistry of Materials*, 1998, **10**, 763-768.
18. M. Avdeev, Z. Mohamed, C. D. Ling, J. Lu, M. Tamaru, A. Yamada and P. Barpanda, *Inorganic chemistry*, 2013, **52**, 8685-8693.
19. S.-M. Oh, S.-T. Myung, J. Hassoun, B. Scrosati and Y.-K. Sun, *Electrochemistry Communications*, 2012, **22**, 149-152.
20. J. L. Allen, T. R. Jow and J. Wolfenstine, *J Solid State Electrochem*, 2008, **12**, 1031-1033.
21. L. Suo, W. Han, X. Lu, L. Gu, Y.-S. Hu, H. Li, D. Chen, L. Chen, S. Tsukimoto and Y. Ikuhara, *Physical Chemistry Chemical Physics*, 2012, **14**, 5363-5367.
22. S. M. Zhang, J. X. Zhang, S. J. Xu, X. J. Yuan and B. C. He, *Electrochimica Acta*, 2013, **88**, 287-293.
23. Y. Zhu, Y. Xu, Y. Liu, C. Luo and C. Wang, *Nanoscale*, 2013, **5**, 780-787.
24. J. X. Zhang, X. Yang, M. S. Zhang, *Functional Materials Letters*, 2011, **4**, 323-326.

25. Y. Fang, L. Xiao, J. Qian, X. Ai, H. Yang and Y. Cao, *Nano letters*, 2014, **14**, 3539-3543.
26. S. Xu, S. Zhang, J. Zhang, T. Tan and Y. Liu, *Journal of Materials Chemistry A*, 2014, **2**, 7221-7228.
27. Y. Liu, S. Xu, S. Zhang, J. Fan and Y. Zhou, *Journal of Materials Chemistry A*, 2015, **2,** 5501-5508
28. V. Mathew, S. Kim, J. Kang, J. Gim, J. Song, J. P. Baboo, W. Park, D. Ahn, J. Han, L. Gu, Y. Wang, Y.-S. Hu, Y.-K. Sun and J. Kim, *NPG Asia Materials*, 2014, **6**, e138-e147.
29. W. Wang, S. Wang, H. Jiao, P. Zhan and S. Jiao, *Physical Chemistry Chemical Physics*, 2015, **17**, 4551-4557.
30. M. Galceran, D. Saurel, B. Acebedo, V. V. Roddatis, E. Martin, T. Rojo and M. Casas-Cabanas, *Physical chemistry chemical physics : PCCP*, 2014, **16**, 8837-8842.
31. H. Kim, J. Hong, K. Y. Park, H. Kim, S. W. Kim and K. Kang, *Chemical reviews*, 2014, **114**, 11788-11827.
32. P. P. Prosini, M. Lisi, S. Scaccia, M. Carewska, F. Cardellini and M. Pasquali, *Journal of The Electrochemical Society*, 2002, **149**, A297-A301.
33. C. M. Julien, *Materials Science and Engineering: R: Reports*, 2003, **40**, 47-102.
34. B. Boonchom and C. Danvirutai, *Industrial & Engineering Chemistry Research*, 2007, **46**, 9071-9076.
35. Y.-m. Zhu, Z.-w. Ruan, S.-z. Tang and V. Thangadurai, *Ionics*, 2014, **20**, 1501-1510.
36. Y. Yin, Y. Hu, P. Wu, H. Zhang and C. Cai, *Chemical Communications*, 2012, **48**, 2137-2139.
37. M. Tang, H. Y. Huang, N. Meethong, Y. H. Kao, W. C. Carter and Y. M. Chiang, *Chemistry of Materials*, 2009, **21**, 1557-1571.
38. Y.-H. Kao, M. Tang, N. Meethong, J. Bai, W. C. Carter and Y.-M. Chiang, *Chemistry of Materials*, 2010, **22**, 5845-5855.
39. B. Guo, H. Ruan, C. Zheng, H. Fei and M. Wei, *Scientific reports*, 2013, **3**.
40. A. Yamada, H. Koizumi, N. Sonoyama and R. Kanno, *Electrochemical and Solid-State Letters*, 2005, **8**, A409-A415.
41. J. L. Dodd, R. Yazami and B. Fultz, *Electrochemical and Solid-State Letters*, 2006, **9**, A151-A155.
42. M. Tang, W. C. Carter, J. F. Belak and Y.-M. Chiang, *Electrochimica Acta*, 2010, **56**, 969-976.

Table 1. Lattice parameters of $NaFePO_4$.

Sintering temp. (°C)	Crystal structure	Space group	*a* (Å)	*b* (Å)	*c* (Å)	α (°)	β (°)	γ (°)	Density (g cm^{-3})
460	olivine	P_{nma}	10.4063	6.2187	4.9469	90	90	90	3.71

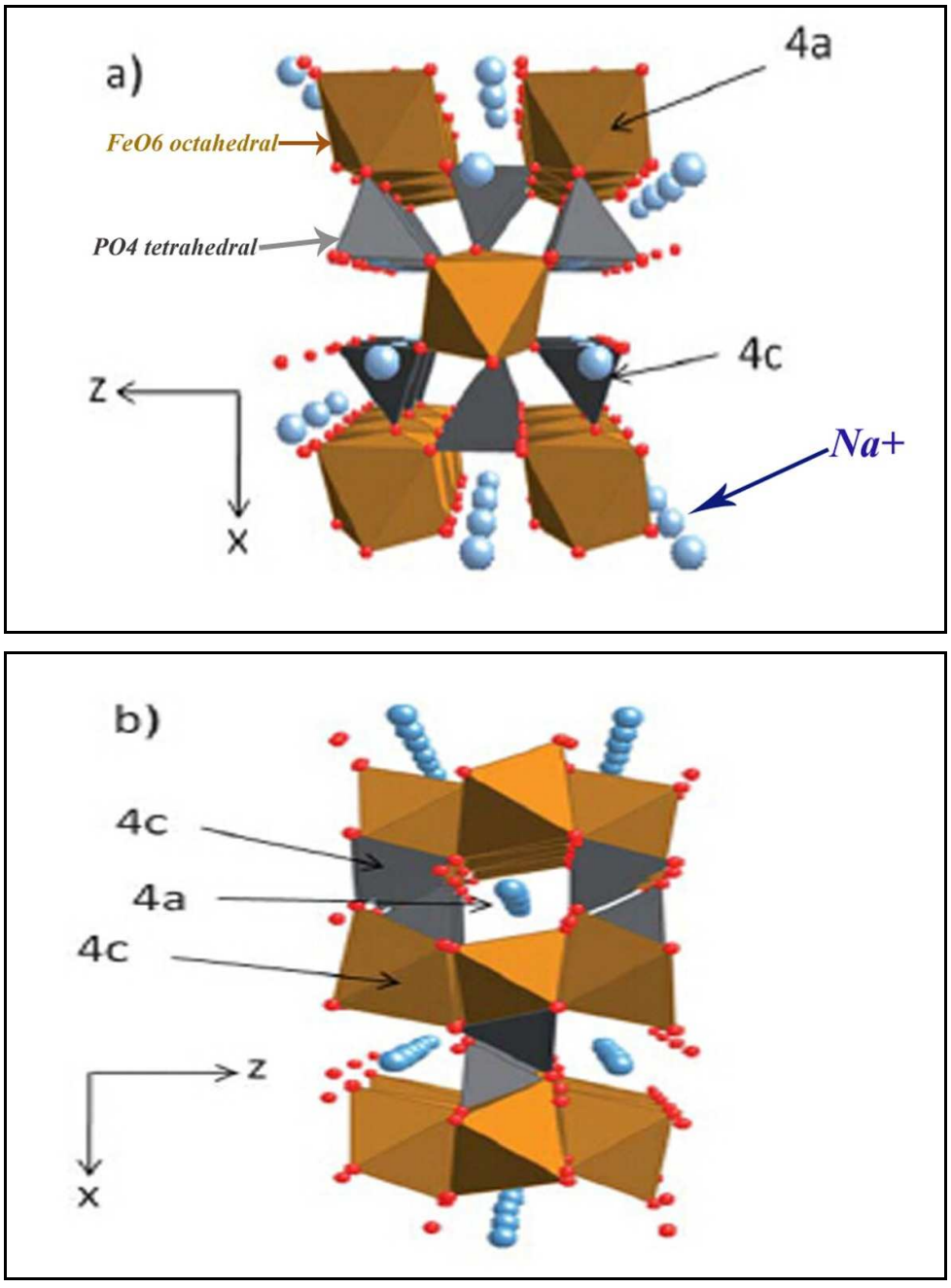

Fig. 1 Crystal structure of $NaFePO_4$: (a) maricite, (b) olivine.

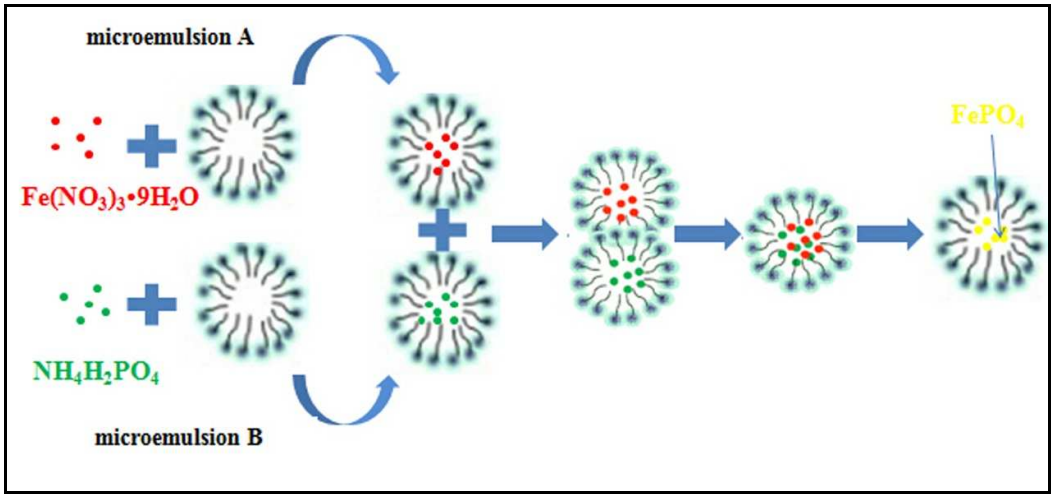

Fig. 2 Schematic of $FePO_4$ nano-particles synthesis

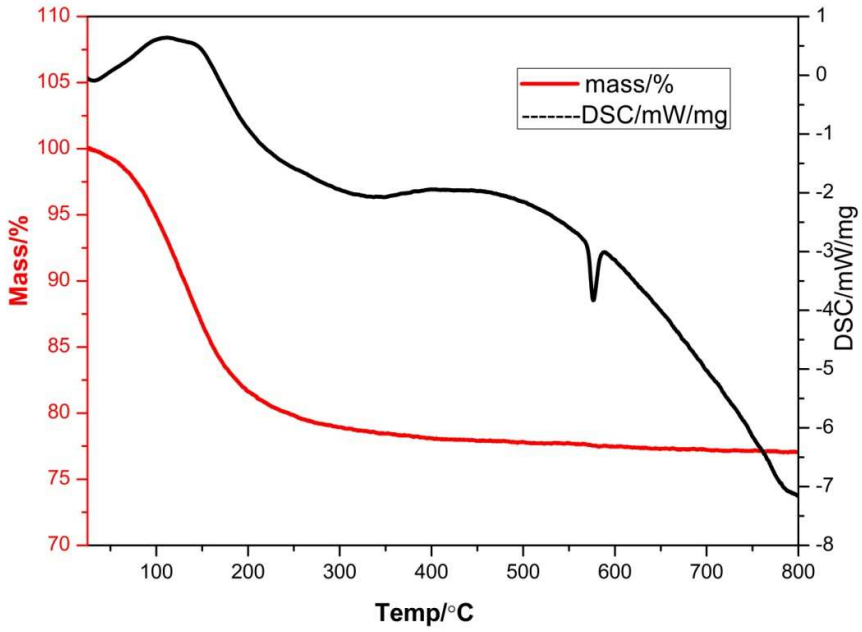

Fig. 3 TGA-DSC of $FePO_4$ nanoparticles.

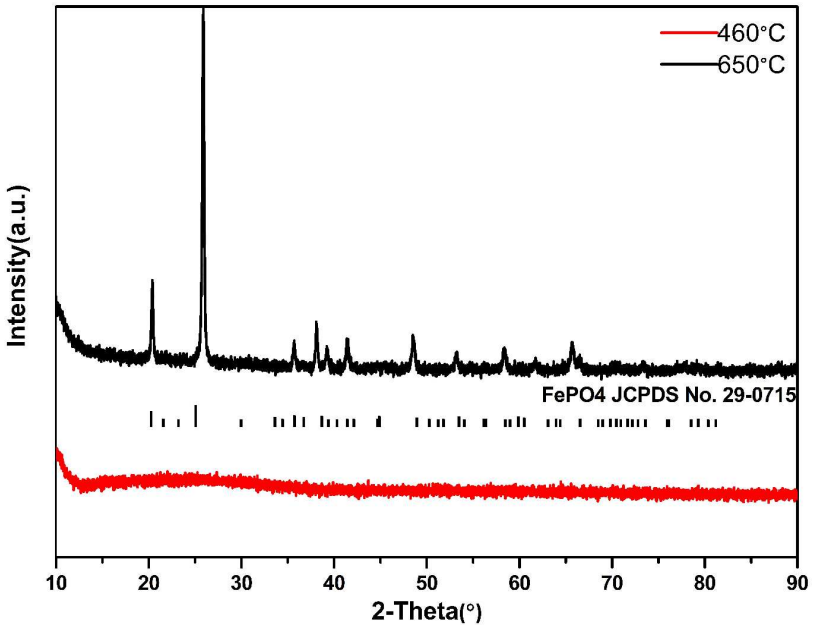

Fig. 4 X-ray diffraction characterization results of $FePO_4$ nanoparticles with sintered at 460°C and 650°C, respectively.

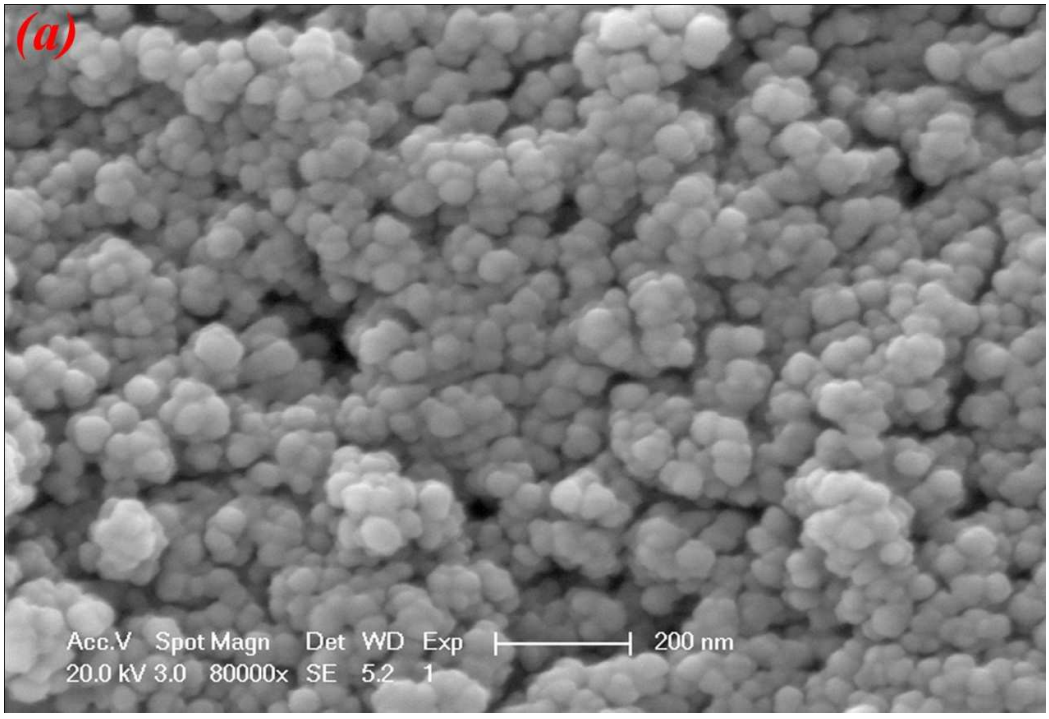

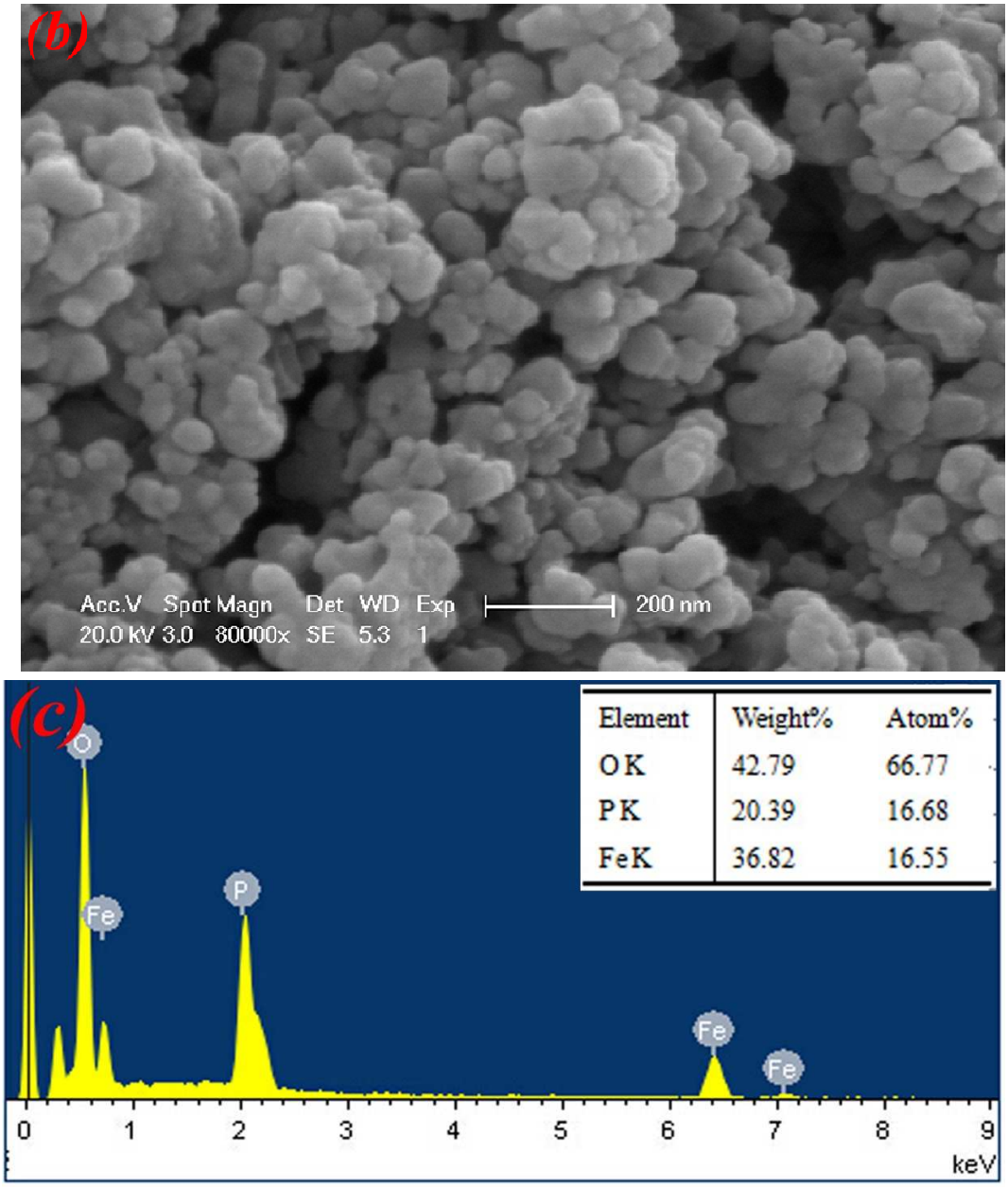

Fig. 5 SEM and EDS images of as-prepared $FePO_4$: (a) 460°C, (b) 650°C, (c) EDS.

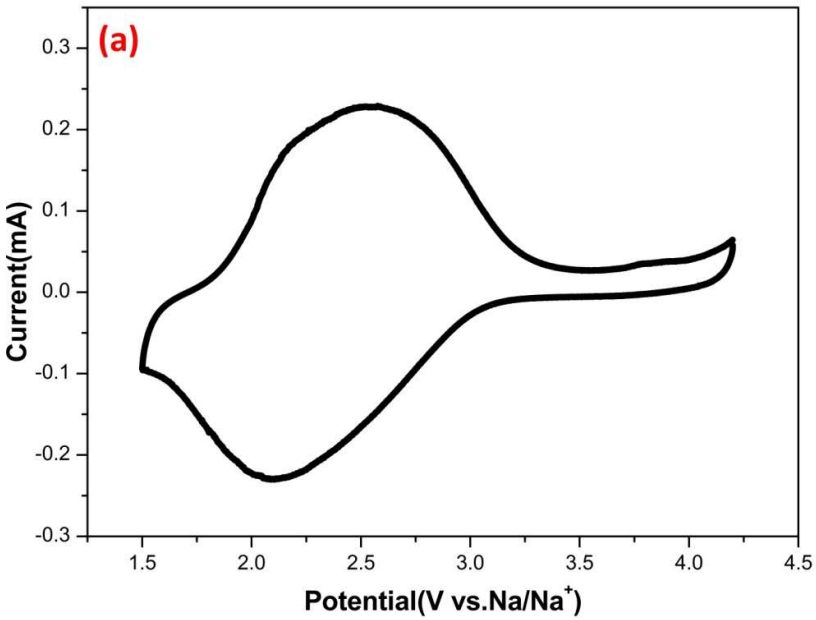

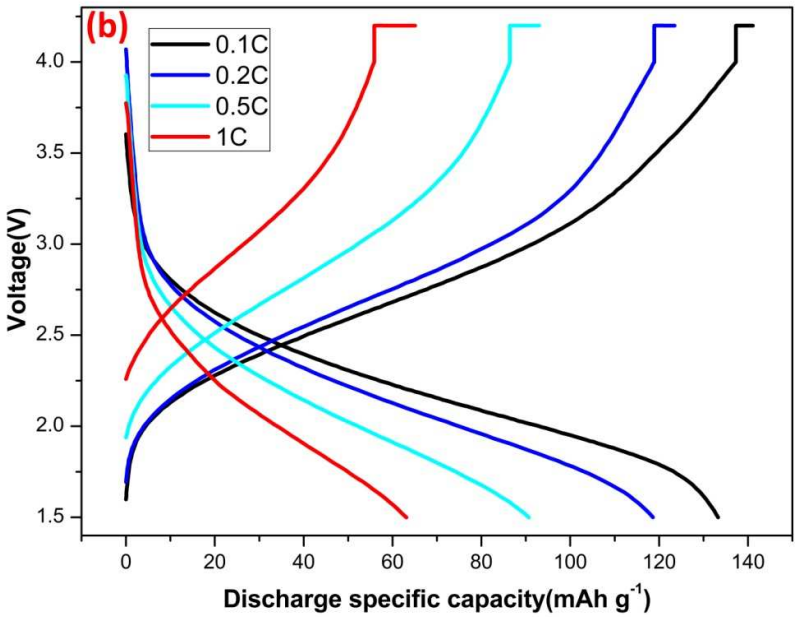

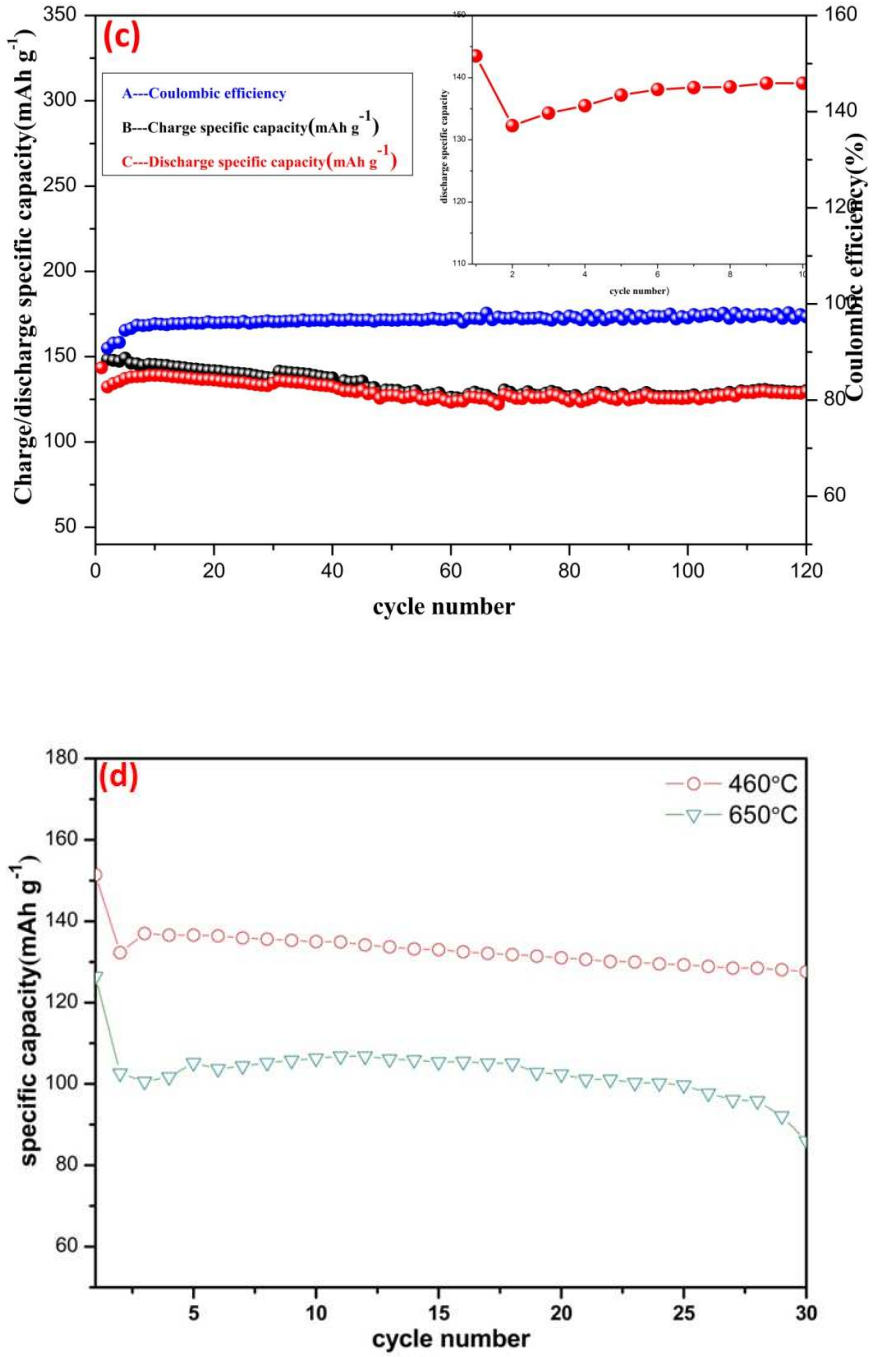

Fig. 6 Electrochemical performance of amorphous $FePO_4$ cathode: (a) CV curve test at scanning rate of 0.05mV s^{-1} (voltage window 1.5-4.2V), (b) rate performance of amorphous $FePO_4$, (c) galvanostatic discharging/charging

profiles performed at 0.1C, and specific-discharge capacity during the initial cycles (c, inset), (d) discharge specific capacity versus cycle numbers of amorphous and hexagonal $FePO_4$ at 0.1 C.

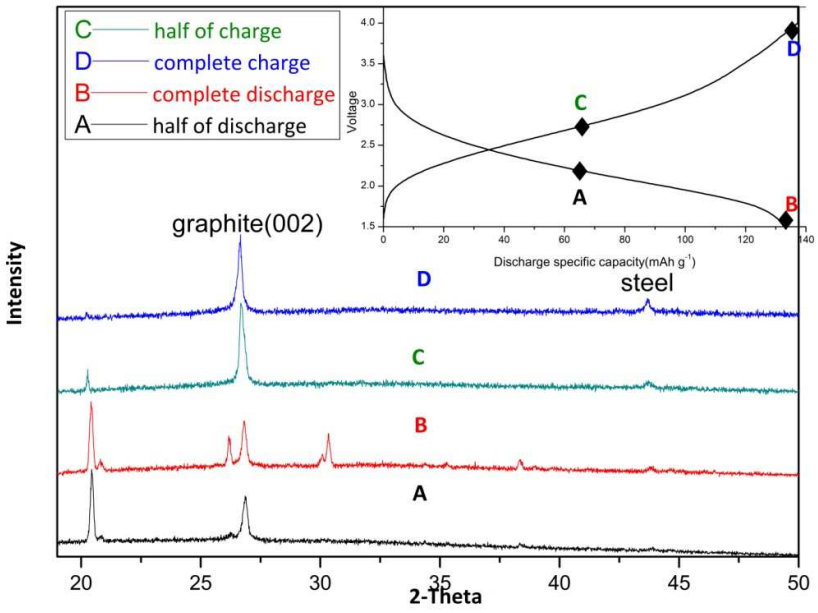

Fig. 7 The XRD patterns of the $FePO_4$ cathode samples taken from the separated sodium half cells at different stages of galvanostatic cycling.

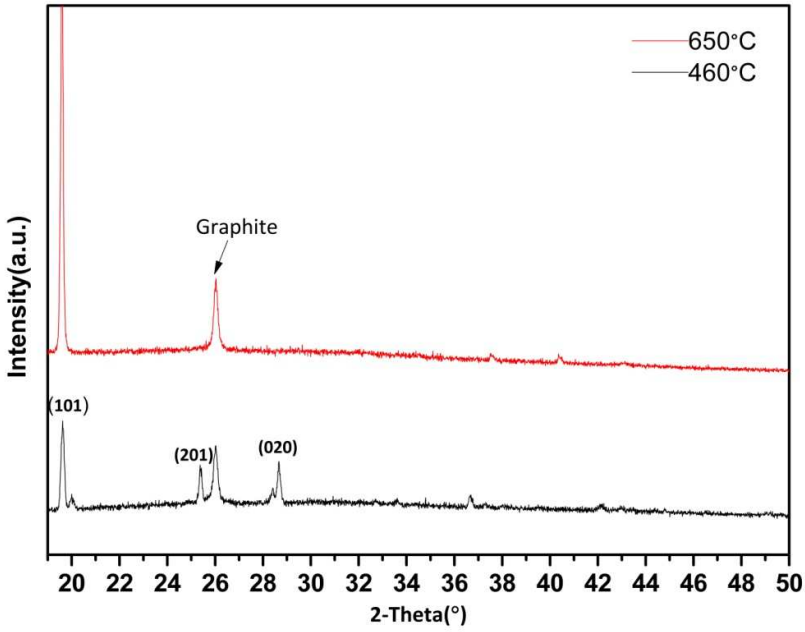

Fig .8 The XRD patterns of the amorphous and hexagonal $FePO_4$ cathode samples at the state of complete discharge.

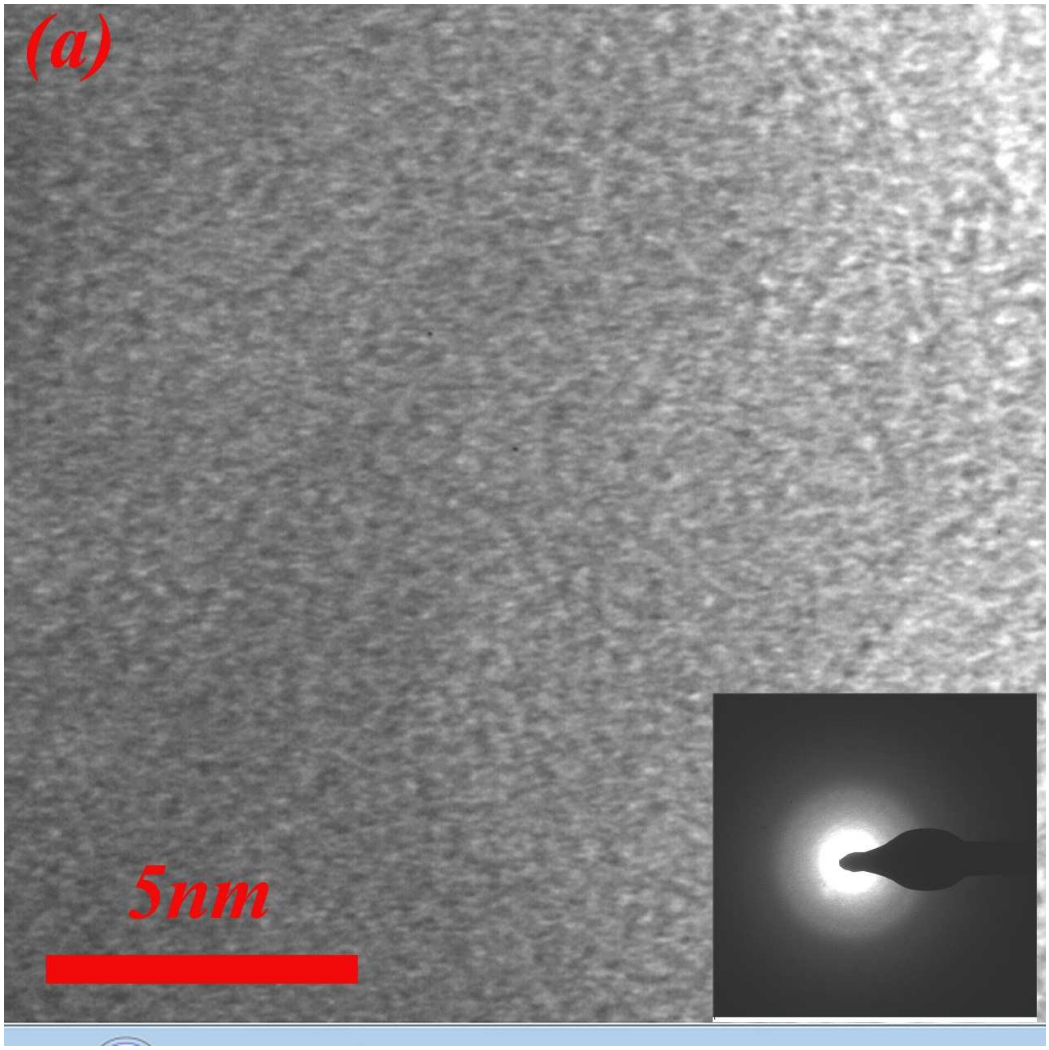

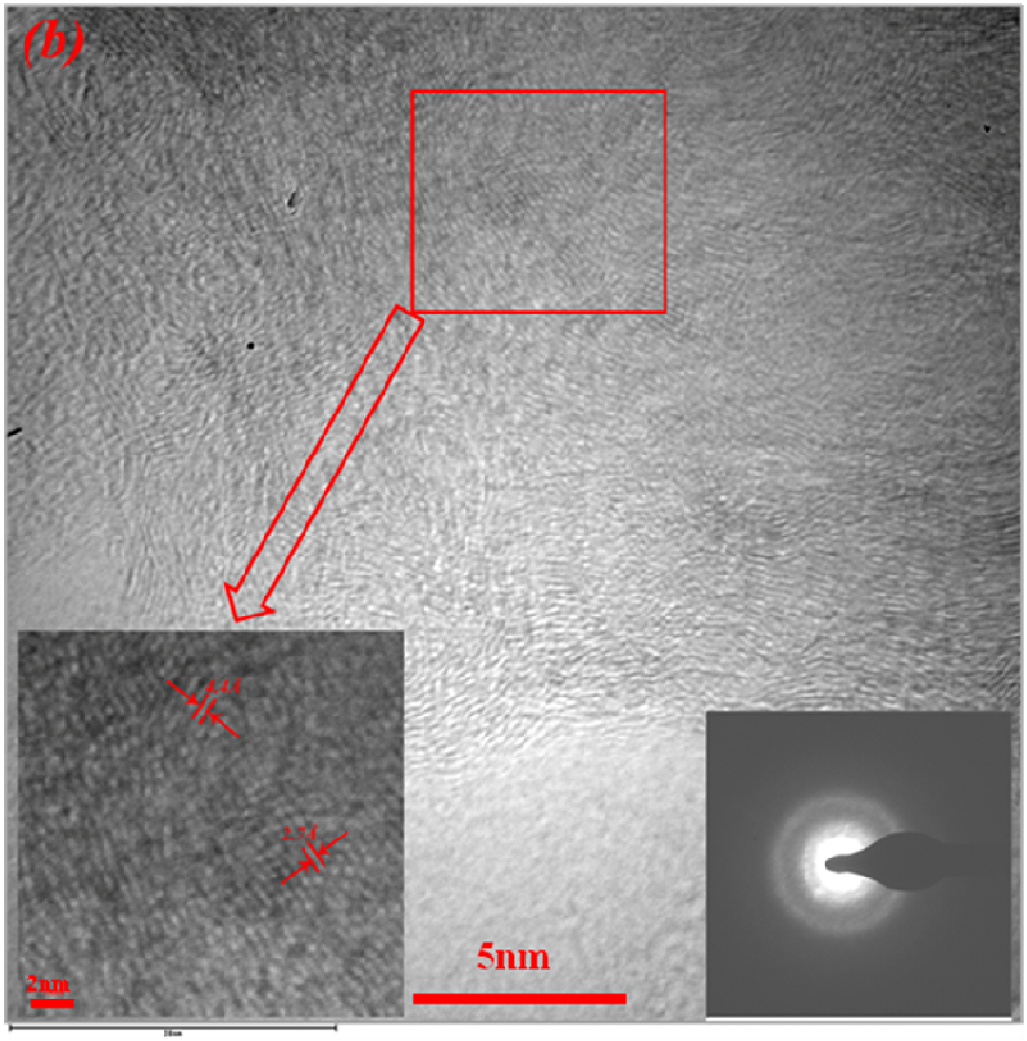

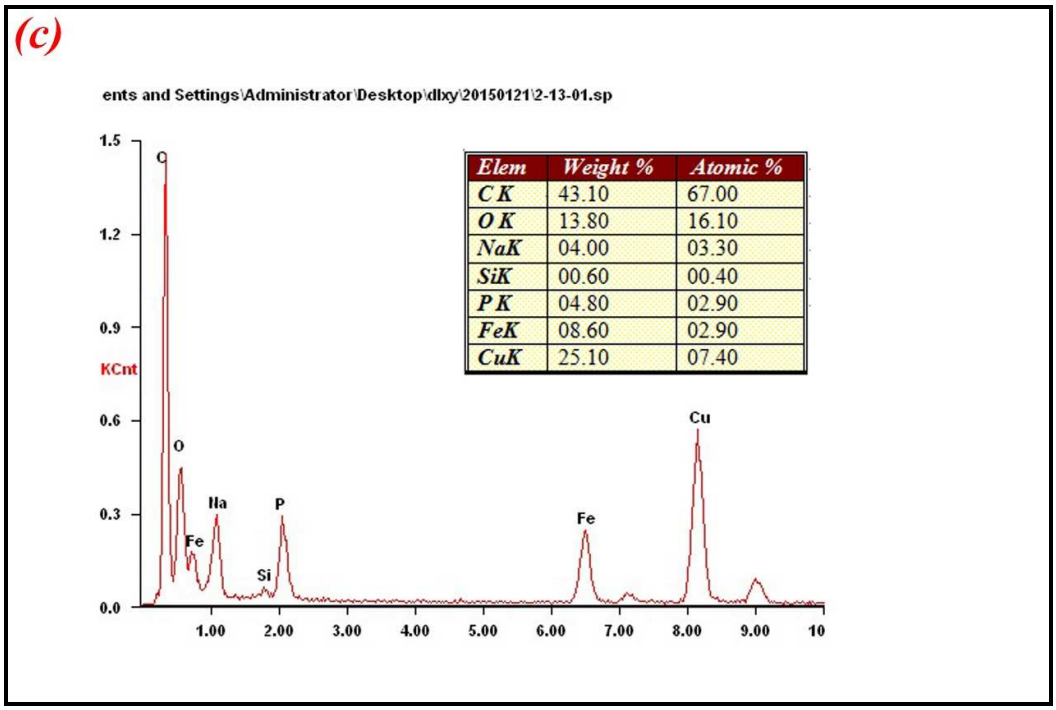

Fig. 9 HRTEM and EDS studies. The HRTEM images of the (a) desodiation/(b)sodiation of amorphous $FePO_4$. The corresponding SAED patterns of the recovered cathode samples are shown in the insets of (a) and (b). (c)The EDS of sodiation amorphous $FePO_4$.

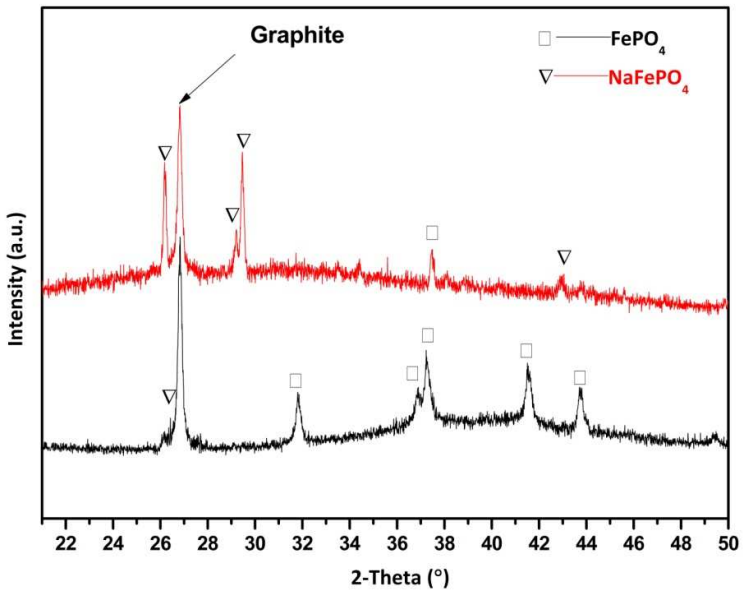

Fig. 10 The XRD patterns of $FePO_4$ and $NaFePO_4$ after many cycles of charging/discharging operation.

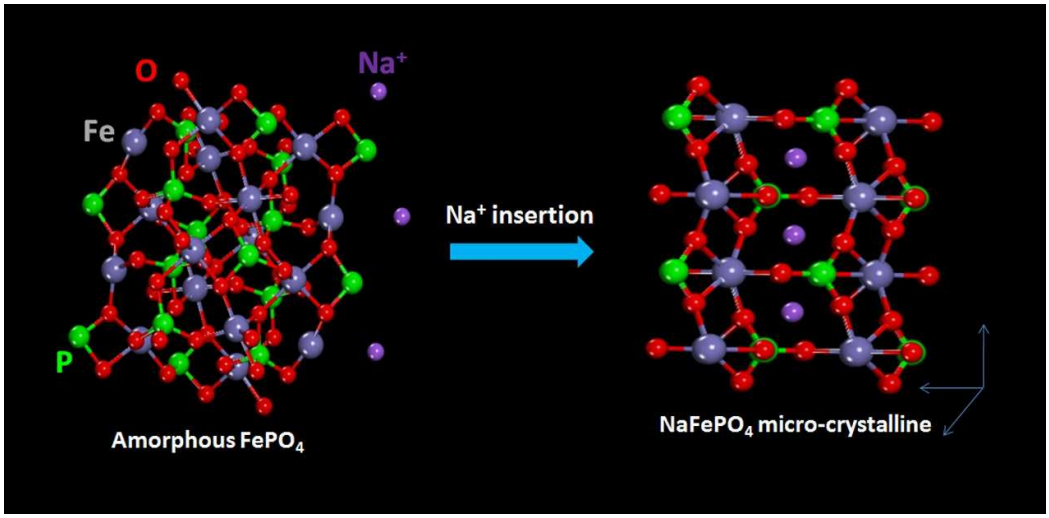

Fig. 11 Schematic illustration of the amorphous to micro-crystalline transition in amorphous $FePO_4$ as cathode material for SIBs during electrochemical sodium-ion insertion.